High-Resolution and Wide-Swath SAR Imaging With Sub-Band Frequency Diverse Array

MENGDI ZHANG
China University of Mining and Technology, China

GUISHENG LIAO, Senior Member, IEEE
JINGWEI XU, Member, IEEE
XIONGPENG HE
Xidian University, China

QI LIU, Member, IEEE
South China University of Technology, China

LAN LAN, Member, IEEE
Xidian University, China

SHIYIN LI
China University of Mining and Technology, China

High-resolution and wide-swath imaging serves as an important task for synthetic aperture radar (SAR). However, the tradeoff between high azimuth resolution and wide unambiguous swath coverage has not been well optimized in traditional SAR system. Meanwhile, the ultrawideband signal is required to obtain ultrahigh range resolution imaging. It is not easy to increase the bandwidth directly due to the difficulty of system design. To this end, this article makes notable contribution on a sub-band frequency diverse array framework to realize range ambiguous echoes separation and wideband signal synthesis from narrowband signals. By introducing a small frequency increment across the elements within each subarray, the transmit steering vector within each subarray is range-angle-dependent, making it feasible to resolve range ambiguity in the spatial frequency. In addition, the transmitted waveforms of different subarrays occupy different frequency bands in range frequency domain, which play a pivotal role in achieving high-resolution imaging. With phase compensation and sub-band frequency spectrum splicing technique, the wideband signal can be obtained. Simulation results have verified the effectiveness of the proposed approach.

Manuscript received 22 June 2021; revised 5 November 2021 and 14 June 2022; accepted 20 June 2022. Date of publication 30 June 2022; date of current version 10 February 2023.

DOI. No. 10.1109/TAES.2022.3187386

Refereeing of this contribution was handled by M. Rice.

This work was supported in part by the National Nature Science Foundation of China under Grant 62101402, in part by the Young Elite Scientists Sponsorship Program by CAST under Grant 2021QNRC001, in part by the China Postdoctoral Science Foundation under Grant 2021M702547, and in part by the Guangdong Provincial Key Laboratory of Human Digital Twin under Grant 2022B1212010004.

Authors' addresses: Mengdi Zhang and Shiyin Li are with the School of Information and Control Engineering, China University of Mining and Technology, Xuzhou 221116, China, E-mail: (zhangmengdi8101@163.com, 0765@cumt.edu.cn); Guisheng Liao, Jingwei Xu, Xiongpeng He, and Lan Lan are with the National Laboratory of Radar signal processing, Xidian University, Xi'an 710071, China, E-mail: (liaogs@xidian.edu.cn; xujingwei1987@163.com; xphe@xidian.edu.cn; lanlan_xidian@foxmail.com); Qi Liu is with the School of Future Technology, South China University of Technology, Guangdong 511442, China, E-mail: (drliuqi@scut.edu.cn). *(Corresponding authors: Mengdi Zhang; Jingwei Xu; Qi Liu.)*

I. INTRODUCTION

Synthetic aperture radar (SAR) is capable of imaging the earth all-weather and all-time, which plays an important role in earth observation applications [1], [2]. As the increase of demand in vast area observation, high-resolution and wide-swath (HRWS) imaging has attracted extensive attention. However, the requirements of pulse repetition frequency (PRF) for wide-swath and high azimuth resolution, respectively, are a world of difference. To be specific, a low PRF is employed to avoid the range ambiguity in wide-swath radar imaging application, while a high PRF is required to address the Doppler ambiguity with the increase of Doppler bandwidth for high azimuth resolution. Therefore, the range ambiguity and Doppler ambiguity problems merit further investigation for HRWS imaging.

Recent researches introduce HRWS imaging technique and can be grouped into two major categories. In the first category, the Doppler ambiguity issue is addressed with azimuth multiple channels or beams, where a low PRF is utilized to guarantee range unambiguity. Displaced phase center antenna (DPCA) technique [7] is proposed, which replaces the synthetic aperture sampling with the real aperture sampling at the equivalent phase center. However, due to the platform motion errors, the DPCA condition is difficult to satisfy in practice. To this end, several methods, such as [8]–[11], have been developed to address the nonuniform displaced phase center sampling problem. In the second category, the range ambiguity is addressed by using space division multiplexing (SDM), frequency division multiplexing (FDM), coding division multiplexing (CDM), and so on. In [12], a multifrequency subpulse mode is proposed, which combines SDM and FDM. On the basis of this mode, each pulse is divided into several subpulses to occupy different frequency bands and these subpulses will irradiate different subswaths to achieve wide coverage. By applying matched filtering, the echoes from different subswaths are separated. In [13]–[18], the azimuth phase coding based on CDM is proposed to suppress the range ambiguity. Nevertheless, its range ambiguity suppression performance is determined by the level of PRF. A high PRF contributes to a good ambiguity suppression performance, and yet reduces the maximum unambiguous range. A method used FDM is proposed in [19], via the range-angle-dependent characteristic of FDA [20]–[22] to separate range ambiguity echoes in the spatial frequency domain. Combining CDM and SDM, some multiple-input multiple-output (MIMO) [23], [24] based methods are proposed to separate the range ambiguous echoes by employing the phase coding in both spatial channels and slow time pulses, such as space-pulse-phase-coding [25], [26] and element-pulse coding [27].

As for the increase of degrees-of-freedom (DOFs), MIMO SAR is attracting the attention of researchers and practitioners alike. Compared with single-input multiple-output and single-input single-output systems, MIMO SAR system can provide more DOFs in space, time, frequency and modulation dimensions. Fully exploiting transmit diversity of MIMO radar is conducive to improving SAR imaging performance, where the orthogonal waveforms are firstly considered to design. The ideal orthogonal waveform satisfies the cross correlation among them for arbitrary shift equals to zero. In light of different realization principles, orthogonal waveforms can be divided into frequency modulation waveforms [28]–[31], Orthogonal frequency division multiplexing (OFDM) waveforms [32]–[34], and orthogonal phase coding waveforms [35]. Frequency modulation waveforms have been implemented in practical radar systems because of its high range resolution. As mentioned in [28], the up-down chirp waveforms are proposed with two orthogonal waveforms and it is extended to four waveforms in [29], named as chirp modulation diversity waveforms. In [30] and [31], the nonlinear frequency modulation waveforms with a continuous piecewise linear instantaneous frequency are designed for MIMO SAR to reduce the transmitting power requirement. Since the conditions of ideal orthogonal waveform is extremely rigorous, short-term shift-orthogonal waveform is proposed in [24]

In this article, a novel sub-band FDA is introduced to realize HRWS SAR imaging where the transmit array is uniformly divided into several subarrays. There is a small frequency increment between the signals transmitted by different elements in the same subarray, and thus, the transmit steering vector per subarray is range-dependent. By performing transmit beamforming, the echoes from different range regions are separated and then unambiguous echoes of wide swath can be obtained. High range resolution means a signal with large bandwidth, which requires a long pulse duration and a high chirp rate. In practice, it is challenging to achieve long time width and high chirp rate simultaneously. To address that, the wideband signal is divided into several narrow band signals by different subarrays. To compensate the phase difference between the echoes emitted by different subarrays, a phase compensation technique is proposed, and then wideband signals are reconstructed by splicing the spectra of the signals corresponding to all subarrays. Finally, the HRWS imaging can be achieved by performing the traditional SAR imaging algorithm. Compared with the conventional FDA, the sub-band FDA has higher degrees of freedom, which are utilized to increase the resolution.

The rest of this article is organized as follows. In Section II, the signal model of sub-band frequency diverse SAR system is presented, followed by an HRWS imaging approach in Section III. In Section IV, some simulation

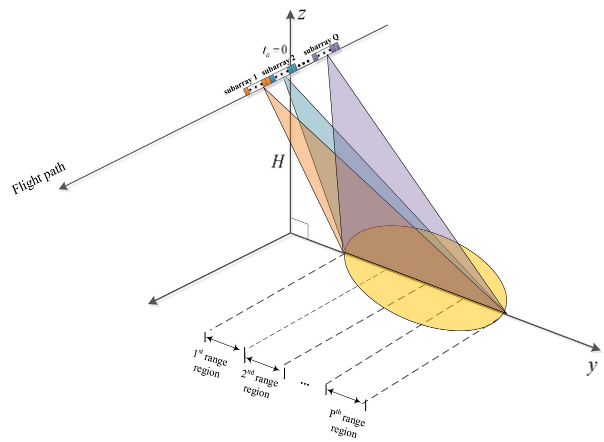

Fig. 1. SAR geometry.

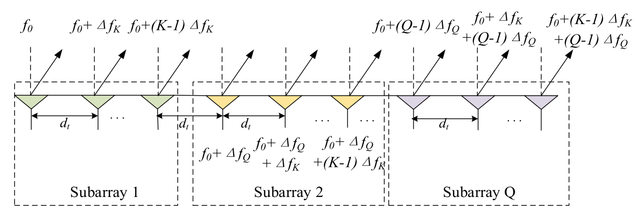

Fig. 2. Configuration of the sub-band frequency diverse array.

results are provided to verify the effectiveness of the proposed method. Finally, Section V concludes this article.

II. SIGNAL MODEL

Without loss of generality, we consider a side-looking SAR geometry, as shown in Fig. 1, where the radar illuminates the observed scene with a wide beam. The velocity of platform is v, and the maximum unambiguous range is R_u. Consider a MIMO radar system consisting of M-antennas transmit uniform linear array (ULA) and N-antennas receive ULA, where the distance between transmit antennas is d_t and distance between receive antennas is d_r. The transmit array is divided into Q regular subarrays and there are K ($K = M/Q$) antennas in each subarray. Note that kth antenna in qth subarray is corresponding to $[K(q-1)+k]$th transmit antenna. The signals are radiated with a small frequency increment Δf_K between adjacent elements within one subarray and a frequency increment Δf_Q between adjacent subarrays, as shown in Fig 2. Δf_Q is slightly less than or equal to the signal bandwidth B_0, which makes the signals transmitted by different subarrays occupy different frequency bands.

Taking the first transmit antenna as the reference element, the carrier frequency at kth element of qth subarray is

$$f_{k,q} = f_0 + \Delta f_m = f_0 + (q-1)\Delta f_Q + (k-1)\Delta f_K \quad (1)$$

where f_0 is the carrier frequency of the first transmit antenna, and Δf_m is the frequency increment of mth ($m = K(q-1)+k$) transmit element.

The signal emitted by kth antenna at qth subarray is

$$s_{k,q}(t_r, t_a) = \text{rect}\left(\frac{t_r}{T_p}\right)\varphi_k(t_r)\exp\left(j2\pi f_{k,q}t\right) \tag{2}$$

where $rect(\frac{t_r}{T_p}) = \begin{cases} 1, |t_r| \le \frac{T_p}{2} \\ 0, |t_r| \ge \frac{T_p}{2} \end{cases}$ represents rectangular range window, $t_r \in (0, T_r)$, t_a, and t $(t = t_r + t_a)$ are the fast time, slow time, and full time, respectively, T_p and T_r denote the pulse duration and the pulse repetition time, respectively, $\varphi_k(t_r)$ is the waveform corresponding to kth antenna of all subarrays. Assume that the waveforms transmitted by the same subarray satisfy the orthogonality condition, i.e.,

$$\int_{T_p} \varphi_k(t_r)\varphi_{k'}^*(t_r - \tau)dt_r = 0, \forall\tau, k \ne k'. \tag{3}$$

The ideal orthogonal waveforms do not exist in practice. Usually, the waveforms are designed to make the cross correlation among them for arbitrary shift approach zero as much as possible in the time domain

The range ambiguity occurs when the swath W_s is wider than R_u and the azimuth ambiguity occurs when the Doppler bandwidth is larger than PRF. In this article, we mainly focus on the range ambiguity resolution issue and we assume the Doppler ambiguity is avoided with a high PRF. Define the range ambiguity number as $P = [\, W_s/R_u]$, where $[\cdot]$ denotes ceiling function. There is a far-field point target on the ground in the pth ($p \in (1, P)$, $p \in N^+$) range region of the imaging scene. After down-conversion, the received baseband signal of the nth receive element is written as

$$\begin{aligned} s_n(t_r, t_a) = \sum_{m=1}^{M} rect\left[\frac{t_r - \tau_{mn}(t_a)}{T_p}\right]\varphi_k\{t_r - \tau_{mn}(t_a)\} \\ \times \exp\{-j2\pi f_0\tau_{mn}(t_a)\} \\ \times \exp\left\{j2\pi\left((q-1)\Delta f_Q + (k-1)\Delta f_K\right)\right. \\ \left.\times (t_r - \tau_{mn}(t_a))\right\} \end{aligned} \tag{4}$$

where $\tau_{mn}(t_a)$ is the round-trip time delay of the signal emitted by the mth ($m = K(q\text{-}1)+k$) transmit element and received by the nth receive element. It is defined as

$$\tau_{mn}(t_a) = \frac{2R(t_a) - (n-1)d_r\sin\theta - (m-1)d_t\sin\theta}{c} \tag{5}$$

in which $R(t_a)$ is the round-trip slant range between the reference element and the target.

Since the signals emitted by each subarray occupy different frequency bands in the frequency domain, the matched filtering is carried out on the mth ($m = K(q\text{-}1)+k$) transmit channel, namely

$$H_m(f_r) = rect\left[\frac{f_r - (q-1)\Delta f_Q - (k-1)\Delta f_K}{B_0}\right]S_{k,q}^*(f_r) \tag{6}$$

where $S_{k,q}(f_r)$ denotes the Fourier transform of $s_{k,q}(t_r, t_a)$.

As shown in Fig. 3, in range-frequency domain, the received signal from mth matched filter of the nth receive antenna is modeled as

$$\begin{aligned} \tilde{S}_{mn}(f_r, t_a) &= H_m(f_r)S_n(f_r, t_a) \\ &= rect\left\{\frac{f_r - \Delta f_m}{\mu T_p}\right\}\varphi_k(f_r - \Delta f_m)\varphi_k^*(f_r - \Delta f_m) \\ &\quad \times \exp(-j2\pi f_0\tau_{mn}) \times \exp(-j2\pi f_r\tau_{mn}). \end{aligned} \tag{7}$$

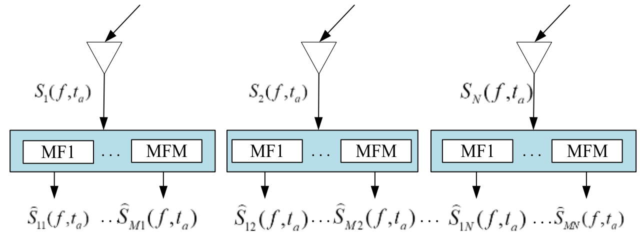

Fig. 3. Signal processing at the receiver with matched filters.

In order to guarantee the spectra of signals from the same subarray with same frequency band, the signal spectrum corresponding to kth element in qth subarray should be shifted by $(k\text{-}1)\Delta f_K$. After the spectrum shift operation, we obtain

$$\begin{aligned} \tilde{S}_{mn}(f_r, t_a) = &rect\left\{\frac{f_r - (q-1)\Delta f_Q}{\mu T_p}\right\}\exp(-j2\pi f_0\tau_{mn}) \\ &\times \varphi_k\{f_r - (q-1)\Delta f_Q\}\varphi_k^*\{f_r - (q-1)\Delta f_Q\} \\ &\times \exp(-j2\pi f_r\tau_{mn})\exp\{-j2\pi(k-1)\Delta f_K\tau_{mn}\} \end{aligned} \tag{8}$$

where μ is the chirp rate of the signal. Taking the range IFFT operation, (8) is written by

$$\begin{aligned} \tilde{s}_{mn}(t_r, t_a) = p_r\{B_0(t_r - \tau_{mn})\}\exp(-j2\pi f_0\tau_{mn}) \\ \times \exp\{-j2\pi(k-1)\Delta f_K\tau_{mn}\} \\ \times \exp\{j2\pi(t_r - \tau_{mn})(q-1)\Delta f_Q\} \end{aligned} \tag{9}$$

where $p_r(\cdot)$ represents the output of matched filter for transmitted waveform. In this article, we follow the commonly-used setting in SAR system, i.e., far-field and spatial narrowband assumption. Inspired by that, the echo envelope variation between array elements can be ignorable for a single pulse. Hence, (9) is approximated by

$$\begin{aligned} \tilde{s}_{mn}(t_r, t_a) \approx p_r\left\{B_0\left(t_r - \frac{2R(t_a)}{c}\right)\right\}\exp\left\{-j4\pi f_0\frac{R(t_a)}{c}\right\} \\ \times \exp\{j2\pi t_r(q-1)\Delta f_Q\} \\ \times \exp\left\{-j4\pi(q-1)\Delta f_Q\frac{R(t_a)}{c}\right\} \\ \times \exp\left\{j2\pi f_0\frac{K(q-1)d_t\sin\theta}{c}\right\} \\ \times \exp\left\{-j4\pi(k-1)\Delta f_K\frac{R(t_a)}{c}\right\} \\ \times \exp\left\{j2\pi f_0\frac{(k-1)d_t\sin\theta}{c}\right\} \\ \times \exp\left\{j2\pi f_0\frac{(n-1)d_r\sin\theta}{c}\right\} \\ \times \exp\left\{j2\pi\left[(q-1)\Delta f_Q + (k-1)\Delta f_K\right]\right. \end{aligned}$$

$$\times \frac{(m-1)d_t \sin\theta}{c}\Bigg\} \times \exp\left\{j2\pi\left[\left(q-1\right)\Delta f_Q + (k-1)\Delta f_K\right] \times \frac{(n-1)d_r \sin\theta}{c}\right\}. \tag{10}$$

Since $f_0 >> (K\text{-}1)\Delta f_K + (Q\text{-}1)\Delta f_Q$, (10) can be further approximated to

$$\begin{aligned}\tilde{s}_{mn}(t_r, t_a) \approx\ & p_r\left\{B_0\left(t_r - \frac{2R(t_a)}{c}\right)\right\}\exp\left\{-j4\pi f_0\frac{R(t_a)}{c}\right\}\\ &\times \exp\left\{j2\pi t_r(q-1)\Delta f_Q\right\}\\ &\times \exp\left\{-j4\pi\left(q-1\right)\Delta f_Q\frac{R(t_a)}{c}\right\}\\ &\times \exp\left\{j2\pi f_0\frac{K\left(q-1\right)d_t\sin\theta}{c}\right\}\\ &\times \exp\left\{-j4\pi\ (k-1)\Delta f_K\frac{R(t_a)}{c}\right\}\\ &\times \exp\left\{j2\pi f_0\frac{(k-1)d_t\sin\theta}{c}\right\}\\ &\times \exp\left\{j2\pi f_0\frac{(n-1)d_r\sin\theta}{c}\right\}.\end{aligned} \tag{11}$$

To summarize, the output signal from the nth receive channel is vectorized as

$$\tilde{\mathbf{s}}_n = \eta\left[\mathbf{b_Q}\left(\theta, R, t_r\right) \otimes \mathbf{b_K}\left(\theta, R\right)\right] \times e^{j2\pi f_0\frac{(n-1)d_r\sin\theta}{c}} \tag{12}$$

where $\tilde{\mathbf{s}}_n \in \mathbb{C}^{KQ\times 1}$ is a snapshot vector corresponding to nth receive channel, $\otimes$ denotes the Kronecker product operation, η denotes the complex amplitude of the target echo, $\mathbf{b_Q}(\theta,R,t_r)\in\mathbb{C}^{Q\times 1}$ and $\mathbf{b_K}(\theta,R)\in\mathbb{C}^{K\times 1}$ are the transmit vectors between subarrays and within subarray, respectively, given by

$$\mathbf{b_Q}\left(\theta, R, t_r\right) = \begin{bmatrix} 1 \\ e^{j2\pi\left(t_r\Delta f_Q - 2\Delta f_Q\frac{R}{c} + f_0\frac{Kd_t\sin\theta}{c}\right)} \\ \vdots \\ e^{j2\pi(Q-1)\left(t_r\Delta f_Q - 2\Delta f_Q\frac{R}{c} + f_0\frac{Kd_t\sin\theta}{c}\right)} \end{bmatrix} \tag{13}$$

and

$$\mathbf{b_K}\left(\theta, R\right) = \begin{bmatrix} 1 \\ e^{j2\pi\left(f_0\frac{d_t\sin\theta}{c} - 2\Delta f_K\frac{R}{c}\right)} \\ \vdots \\ e^{j2\pi(K-1)\left(f_0\frac{d_t\sin\theta}{c} - 2\Delta f_K\frac{R}{c}\right)} \end{bmatrix}. \tag{14}$$

From (13), we observe that the transmit steering vector between subarrays is dependent on range, angle, and time. It can be written as

$$\mathbf{b_Q}\left(\theta, R, t_r\right) = \mathbf{d_Q}\left(\theta\right) \odot \mathbf{r_Q}\left(t_r, R\right) \tag{15}$$

where $\odot$ denotes the Hadamard product. $\mathbf{d_Q}(\theta)$ and $\mathbf{r_Q}(t_r,R)$ are the angle and range-time transmit steering vector, respectively, between subarrays

$$\mathbf{d_Q}\left(\theta\right) = \left[\ 1\ e^{j2\pi f_0\frac{Kd_t\sin\theta}{c}}\ \cdots\ e^{j2\pi(Q-1)f_0\frac{Kd_t\sin\theta}{c}}\ \right]^T \tag{16}$$

and

$$\mathbf{r_Q}\left(t_r, R\right) = \left[1\ e^{j2\pi\left(t_r\Delta f_Q - 2\Delta f_Q\frac{R}{c}\right)} \cdots e^{j2\pi(Q-1)\left(t_r\Delta f_Q - 2\Delta f_Q\frac{R}{c}\right)}\right]^T. \tag{17}$$

Due to the range-time vector $\mathbf{r_Q}(t_r,R)$, the signals corresponding to different subarrays occupy different sub-bands, which is the foundation for synthesizing these signals to acquire a large bandwidth.

From (14), the transmit vector within subarray is dependent on range and angle, which can be written as

$$\mathbf{b_K}\left(\theta, R\right) = \mathbf{d_K}\left(\theta\right) \odot \mathbf{r_K}\left(R\right) \tag{18}$$

where $\mathbf{d_K}(\theta)$ and $\mathbf{r_K}(R)$ are the angle and range transmit vectors within subarray, respectively, and they are

$$\mathbf{d}_K\left(\theta\right) = \left[\ 1\ e^{j2\pi f_0\frac{d_t\sin\theta}{c}}\ \cdots\ e^{j2\pi(K-1)f_0\frac{d_t\sin\theta}{c}}\ \right]^T \tag{19}$$

and

$$\mathbf{r_K}\left(R\right) = \left[\ 1\ e^{-j4\pi\Delta f_K\frac{R}{c}}\ \cdots\ e^{-j4\pi(K-1)\Delta f_K\frac{R}{c}}\ \right]^T. \tag{20}$$

Utilizing the range and angle dependence of the transmit steering vector within subarray, it is capable of forming range-dependent transmit beampattern within subarray to separate ambiguous echoes.

Stacking the output vectors from all N receive channels, we obtain the snapshot of the echo as

$$\begin{aligned}\tilde{\mathbf{s}} &= \left[\ \tilde{\mathbf{s}}_1^T\ \tilde{\mathbf{s}}_2^T\ \cdots\ \tilde{\mathbf{s}}_N^T\ \right]^T\\ &= \eta\mathbf{a}\left(\theta\right) \otimes \left[\mathbf{b_Q}\left(\theta, R, t_r\right) \otimes \mathbf{b_K}\left(\theta, R\right)\right]\end{aligned} \tag{21}$$

where $\tilde{\mathbf{s}}\in\mathbb{C}^{NKQ\times 1}$ is the snapshot vector and $\mathbf{a}(\theta)\in\mathbb{C}^{N\times 1}$ is the receive vector, namely

$$\mathbf{a}\left(\theta\right) = \left[\ 1\ e^{j2\pi f_0\frac{d_r\sin\theta}{c}}\ \cdots\ e^{j2\pi f_0\frac{(N-1)d_r\sin\theta}{c}}\ \right]^T. \tag{22}$$

To achieve signal gain of the full aperture, receive beamforming is first performed on the echo signal after matched filtering. Thus, the output signal of receive beamformer is expressed as

$$\begin{aligned}\breve{\mathbf{s}} &= \left[\mathbf{a}\left(\theta_0\right) \otimes \left(I_\mathbf{Q} \otimes I_\mathbf{K}\right)\right]^H\tilde{\mathbf{s}}\\ &= \xi\mathbf{b_Q}\left(\theta, R\right) \otimes \mathbf{b_K}\left(\theta, R\right)\\ &= \left[\ \breve{\mathbf{s}}_1^T\ \breve{\mathbf{s}}_2^T\ \cdots\ \breve{\mathbf{s}}_Q^T\ \right]^T\end{aligned} \tag{23}$$

where ξ is the complex amplitude, $\breve{\mathbf{s}}\in\mathbb{C}^{KQ\times 1}$ is the snapshot vector after receive beamforming, $\mathbf{I}_Q\in\mathbb{C}^{Q\times Q}$ and $\mathbf{I}_K\in\mathbb{C}^{K\times K}$ are the unit matrices, and $\breve{\mathbf{s}}_q\in\mathbb{C}^{K\times 1}$ is the snapshot vector of qth subarray, which can be written as

$$\breve{\mathbf{s}}_q = \zeta_q\mathbf{g}_q\left(\theta, R\right). \tag{24}$$

Herein, ζ_q and $\mathbf{g}_q(\theta,R)\in\mathbb{C}^{K\times 1}$ denote the complex amplitude and the transmit steering vector corresponding to

qth subarray, respectively. They can be expressed as

$$\zeta_q = \xi p_r \left(t_r + \left(p-1\right) T_r - \frac{2R(t_a)}{c} \right) \exp\left\{ -j4\pi f_0 \frac{R(t_a)}{c} \right\} \times \exp\left\{ j2\pi \left(t_r - \frac{2R(t_a)}{c} \right) (q-1)\Delta f_Q \right\} \tag{25}$$

and

$$\begin{aligned} \mathbf{g}_q(\theta, R) &= d_q(\theta)\mathbf{b}_\mathbf{K}(\theta, R) \\ &= \exp\left\{ j2\pi f_0 \frac{K(q-1)d\sin\theta}{c} \right\} \\ &\times \begin{bmatrix} 1 \\ \mathrm{e}^{-j4\pi\Delta f_K \frac{R}{c} + j2\pi f_0 \frac{d\sin\theta}{c}} \\ \vdots \\ \mathrm{e}^{-j4\pi(K-1)\Delta f_K \frac{R}{c} + j2\pi(K-1) f_0 \frac{d\sin\theta}{c}} \end{bmatrix}. \end{aligned} \tag{26}$$

III. HIGH-RESOLUTION AND WIDE-SWATH SAR IMAGING

In this section, a HRWS imaging method is proposed, where a range ambiguity suppression approach based on unambiguous signal reconstruction for FDA [19] is presented in subarray level.

It can be seen from (26) that the transmit steering vector within subarray is range-dependent. Therefore, the signals of desired range region are required to extract via transmit beamforming in spatial frequency domain. Define the transmit spatial frequency as

$$f_T = -2\Delta f_K \frac{R}{c} + f_0 \frac{d\sin\theta}{c}. \tag{27}$$

Let l as the index of range bin, and thus, the slant range of the scatter in the lth range bin of the pth range region is

$$R = R_l + (p-1)R_u \tag{28}$$

where R_l denotes the closest slant range of the lth range bin in the first range region. Using (28), (27) is rewritten as

$$f_T = -2\Delta f_K \frac{R_l}{c} - 2\Delta f_K \frac{\left(p-1\right)R_u}{c} + f_0 \frac{d\sin\theta}{c}. \tag{29}$$

In order to make the spatial frequency of targets in different range regions do not overlap, the first term in (29) varying with different range bins, should be compensated. Hence, the range dependence compensation function is constructed as

$$\mathbf{h}_l = \left[1 \; e^{j4\pi\Delta f_K \frac{R_l}{c}} \; \ldots \; \mathrm{e}^{j4\pi\Delta f_K \frac{(k-1)R_l}{c}} \right]^T. \tag{30}$$

Applying the compensation steering vector to the transmit steering vector, we have

$$\begin{aligned} &\hat{\mathbf{g}}_q^H\left(\theta, (p-1)R_u\right) = \mathbf{g}_q^H(\theta, R) \odot h_l \\ &= \mathrm{e}^{j2\pi f_0 \frac{K(q-1)d\sin\theta}{c}} \times \begin{bmatrix} 1 \\ e^{-j4\pi\Delta f_K \frac{(p-1)R_u}{c} + j2\pi f_0 \frac{d\sin\theta}{c}} \\ \vdots \\ e^{-j4\pi(K-1)\Delta f_K \frac{(p-1)R_u}{c} + j2\pi(K-1) f_0 \frac{d\sin\theta}{c}} \end{bmatrix}. \end{aligned} \tag{31}$$

The echoes after compensation can be expressed as

$$\hat{\mathbf{s}}_q = \sum_i \xi_{q,i} \hat{\mathbf{g}}_q(\theta_i, (p_i-1)R_u) \tag{32}$$

where i is the index of target number.

To separate the ambiguous echoes per range region, a series of weight vectors are constructed to enhance the signal power of desired range region and to suppress the ambiguous signals from the rest range regions. The constraint condition for designing this weight vector is summarized as

$$\begin{cases} \min\limits_{\mathbf{w}_{q,p}} \mathbf{w}_{q,p}^H \mathbf{R}_{q,-p} \mathbf{w}_{q,p} \\ \mathbf{w}_{q,p} \hat{\mathbf{g}}_q(\theta_0, (p-1)R_u) = 1 \end{cases}, \; p = 1, 2, \cdots P \tag{33}$$

where $\mathbf{w}_{q,p}$ is the weight vector of the qth subarray for the pth range region, p is the index of the desired range region, and $\mathbf{R}_{q,-p}$ is the covariance matrix of the echo corresponding to qth subarray without the desired range region and it can be expressed as

$$\mathbf{R}_{q,-p} = \sum_{s=1, s\neq p}^{P} \sigma_s^2 \hat{\mathbf{g}}_q(\theta_0, (s-1)R_u) \hat{\mathbf{g}}_q^H(\theta_0, (s-1)R_u). \tag{34}$$

By solving the constraint condition in (33), we can get the weight vector as

$$\mathbf{w}_{q,p} = \frac{\mathbf{R}_{q,-p}^{-1} \hat{\mathbf{g}}_q(\theta_0, (p-1)R_u)}{\hat{\mathbf{g}}_q^H(\theta_0, (p-1)R_u) \mathbf{R}_{q,-p}^{-1} \hat{\mathbf{g}}_q(\theta_0, (p-1)R_u)}. \tag{35}$$

Applying the transmit weight vector $\mathbf{w}_{q,p}$ to the signal corresponding to qth subarray, the signal from pth range region corresponding to qth subarray is expressed as

$$\bar{s}_{q,p} = \mathbf{w}_{q,p}^H \hat{\mathbf{s}}_q. \tag{36}$$

Performing the transmit beamforming on all range regions and all subarrays, a $P \times Q$ complex matrix that contains the resolved unambiguous echoes of full swath can be obtained as

$$\bar{\mathbf{S}} = \left[\bar{\mathbf{S}}_1 \; \bar{\mathbf{S}}_2 \; \ldots \; \bar{\mathbf{S}}_Q \right] \tag{37}$$

where $\bar{\mathbf{S}}_q \in \mathbb{C}^{P\times 1}$ denotes the complex matrix corresponding to qth subarray of full swath and is written as

$$\bar{\mathbf{S}}_q = \left[\bar{s}_{q,1} \; \bar{s}_{q,2} \; \ldots \; \bar{s}_{q,P} \right]^T. \tag{38}$$

Transforming $\bar{s}_{q,p}$ in (36) into the range-frequency domain, we get

$$\begin{aligned} \bar{S}_{q,p}(f_r, t_a) &= \mathrm{rect}\left[\frac{f_r - (q-1)\Delta f_Q}{B_0} \right] W\left(f_r\right) \\ &\times \exp\left\{ -j2\pi(q-1)(p-1)\Delta f_Q T_r \right\} \\ &\times \exp\left(-j2\pi f_0 \frac{2R(t_a)}{c} \right) \end{aligned} \tag{39}$$

in which

$$\begin{aligned} W\left(f_r\right) &= \varphi\left\{ f_r - (q-1)\Delta f_Q \right\} \varphi^*\left\{ f_r - (q-1)\Delta f_Q \right\} \\ &\times \exp\left\{ -j2\pi f_r \left(\frac{2R(t_a)}{c} - (p-1)T_r \right) \right\}. \end{aligned} \tag{40}$$

Then, a spectrum splicing method is proposed to achieve high-resolution SAR imaging. The wideband signal can be obtained by combining the signals corresponding to all subarrays. The bandwidth of the combined wideband signals is $B = B_0+(Q\text{-}1)\ \Delta f_Q$. Before spectrum splicing, the redundant phase caused by the frequency increment Δf_Q between subarrays should be compensated. The phase compensation function is expressed as

$$\bar{h}_{q,p} = \exp\left\{j2\pi \Delta f_Q (q-1)(p-1)T_r\right\}. \tag{41}$$

Applying (41) to (39), we have

$$\bar{S}_{com-q,p}(f_r, t_a) = \mathrm{rect}\left[\frac{f_r-(q-1)\Delta f_Q}{B_0}\right] W\left(f_r\right) \times \exp\left(-j2\pi f_0 \frac{2R(t_a)}{c}\right) \tag{42}$$

Case I: $\Delta f_Q = B_0$.

In this case, the frequency sub-bands of signals corresponding to qth subarrays are adjacent to the ones corresponding to $(q+1)$th subarray in the range frequency domain. After spectrum splicing, the signal bandwidth becomes Q times of the original one

$$\begin{aligned}\bar{S}_{\text{wide}-p}(f_r, t_a) &= \sum_{q=1}^{Q} \bar{S}_{q,p}(f_r, t_a) \\ &= \mathrm{rect}\left[\frac{\mathrm{f_r}}{\mathrm{QB_0}}\right] \mathrm{W}\left(\mathrm{f_r}\right) \exp\left(-\mathrm{j}2\pi \mathrm{f_0} \frac{2\mathrm{R}(\mathrm{t_a})}{\mathrm{c}}\right)\end{aligned} \tag{43}$$

Case II: $\Delta f_Q < B_0$.

In this case, the spectra of signals corresponding to adjacent subarrays are overlapped, where the spectra from qth and $(q+1)$th subarrays are overlapped at $[q\Delta f_Q, B_0+(q\text{-}1)\Delta f_Q]$ in the range frequency domain. Thus, the wideband signal corresponding to pth range region can be synthesized by

$$\begin{aligned}\bar{S}_{\text{wide}-p}(f_r, t_a) &= \sum_{q=1}^{Q} \bar{S}_{q,p}(f_r, t_a) - \frac{1}{2}\sum_{q=1}^{Q} \\ &\quad \times \mathrm{rect}\left[\frac{f_r - q\Delta f_Q}{B_0 - \Delta f_Q}\right] \bar{S}_{q,p}(f_r, t_a) \\ &= \mathrm{rect}\left[\frac{f_r}{B_0+(Q-1)\,\Delta f_Q}\right] W\left(f_r\right) \\ &\quad \times \exp\left(-j2\pi f_0 \frac{2R(t_a)}{c}\right).\end{aligned} \tag{44}$$

As shown in Fig. 4, the procedure of the proposed method is summarized. The received signals are processed by matched filters in range frequency domain to recover the DOFs of transmitter. To guarantee the signals from same transmit subarray with same frequency band in the range-frequency domain, their spectra are shifted. After spectrum shifting, receive beamforming is performed on the signals

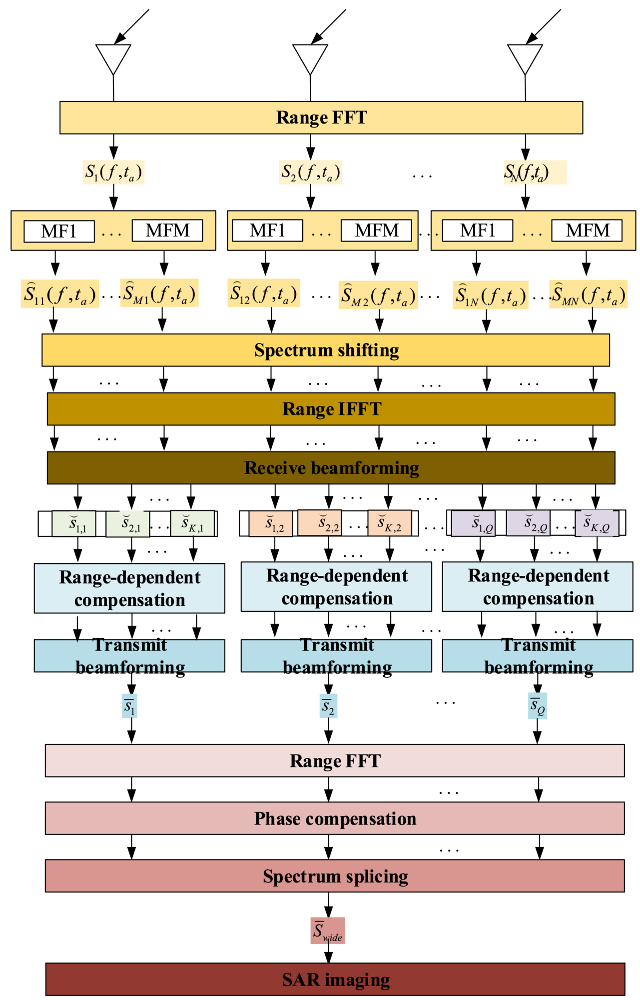

Fig. 4. Procedure of HRWS SAR imaging.

to acquire the full-aperture gain. Next, the ambiguous signals can be separated by range-dependent compensation and transmit beamforming procedures. Subsequently, the wideband signals are obtained by phase compensation and spectrum splicing. Finally, the HRWS imaging results of full swath can be obtained by performing traditional SAR imaging algorithm.

The proposed method enhances the capability of high-resolution imaging in the HRWS system, while increases the complexity of the HWRS system. To alleviate this issue, we have the following points. First, the range ambiguity resolution procedure is realized by equivalent transmit beamforming which is applied after receive the echo and multiple waveforms separation. This equivalent transmit beamforming procedure can be realized using online DBF technique, resulting in separated echoes corresponding to different range regions. Second, the receive degrees of freedom is still preserved, which can be otherwise used for other purpose, such moving target indication, parameter estimation, *et al.* Thus, the receive channel number can be designed accordingly. In this article, the receive channel number N can be set as one, which has no influence on range ambiguity resolution and multiband spectrum splicing. In

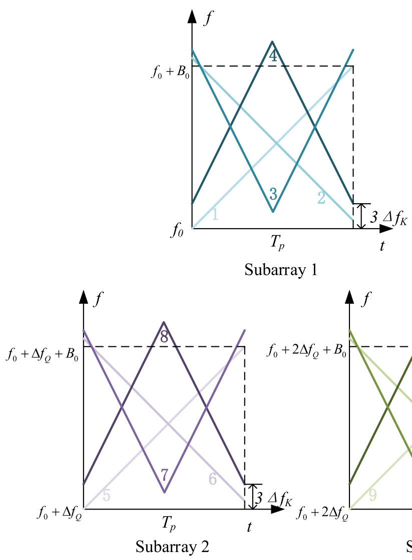

Fig. 5. Time-frequency illustrations of OFDM chirp modulation waveforms.

other words, the proposed HRWS imaging method is still feasible with only one receive channel.

IV. SIMULATION

A. Imaging Simulations on Point Target

In this part, a ULA with 12 transmit and receive elements is considered, where the transmit array is divided into 3 regular subarrays. The carrier frequencies of transmitted signals are f_0, $f_0+\Delta f_K$, $f_0+2\Delta f_K$, $f_0+3\Delta f_K$, $f_0+\Delta f_Q$, $f_0+\Delta f_Q+\Delta f_K$, $f_0+\Delta f_Q+2\Delta f_K$, $f_0+\Delta f_Q+3\Delta f_K$, $f_0+2\Delta f_Q$, $f_0+2\Delta f_Q+\Delta f_K$, $f_0+2\Delta f_Q+2\Delta f_K$, and $f_0+2\Delta f_Q+3\Delta f_K$, respectively. Chirp modulation diversity waveform is applied for the following simulation, as shown in Fig. 5. To evaluate the imaging performance of the proposed framework, three range regions, including nine targets each range region in mainbeam are considered. The sample numbers in range and azimuth are 4800 and 2000, respectively. Thus, the scene centers of all range regions are corresponding to the 2400th sample numbers in range and 1000th sample numbers in azimuth. The point targets of the first, second, and third range regions are distributed within ± 150, ± 600, and ± 300 range bins from the centers. Table I lists the key used parameters of the proposed SAR imaging system.

After matched filtering, the signals corresponding to different transmit arrays can be separated. Fig. 6(a) shows the signal received by the first array and transmitted by the first antenna in the first subarray. It is observed that the echoes from all range regions are mixed due to the range ambiguity. By performing transmit beamforming with the beamformer designed for the first range region, the echoes of the first range region can be extracted from the range ambiguous echoes, as shown in Fig. 6(b). It can be seen that the range ambiguous energies of the second and third range regions have been well suppressed. Similarly, with the beamformers designed for the second and third range regions, the echoes of the second and third range regions can be abstracted in Fig. 6(c) and (d), respectively.

TABLE I
System Parameters

Symbol	Parameter	Value
f_0	Carrier frequency	5.3 GHz
B_0	Bandwidth	70 MHz
T_p	Pulse width	10 μs
N	Number of receive elements	12
M	Number of transmit elements	12
Q	Number of subarrays	3
Δf_K	Frequency increment in subarray	1 MHz
Δf_Q	Frequency increment between adjacent subarray	66 MHz
F_r	Fast time sampling frequency	240 MHz
prf	Pulse repetition frequency	4400 Hz
B_d	Doppler bandwidth	3800 Hz
v	Platform velocity	7600 m/s
H	Platform Height	530 Km

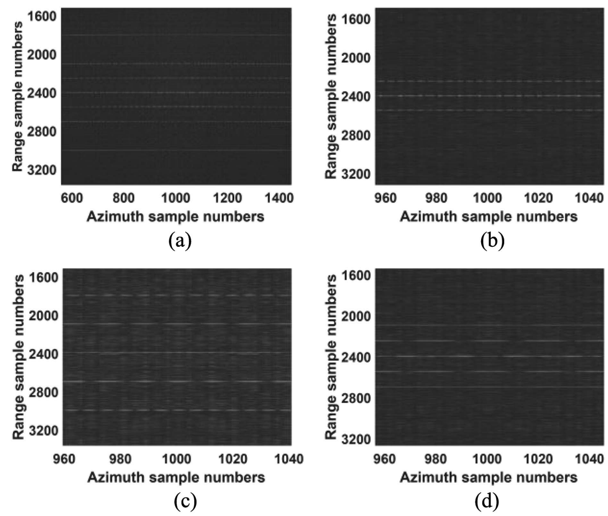

Fig. 6. Signal after range compensation. (a) Original signal. (b) Signal from first range region after transmit beamforming. (c) Signal from second range region after transmit beamforming. (d) Signal from third range region after transmit beamforming.

In Fig. 7, the spectra of the echoes per subarray from the first range region in range-frequency domain are plotted, where Fig. 7(a)–(c) display the signal spectra of 1000th pulse with respect to first, second, and third subarrays, respectively. The wideband signal of 202 MHZ is obtained by phase compensation and spectrum splicing, seen from Fig. 7(d).

To demonstrate the HWRS imaging performance of the proposed scheme, we have conducted simulations on first, second, and third, respectively, in Fig. 8. Additionally, Fig. 9 shows the range profile and azimuth profile in first range region, where PSLRs (ISLRs) of the target in range and azimuth profiles are -13.25 dB (-11.57 dB) and -19.48 dB (-11.96 dB), respectively. Moreover, it is concluded that the range resolution and azimuth resolution are 0.76 m and 2.03 m, while the theoretical resolution in range and azimuth are 0.74 m and 2 m, respectively.

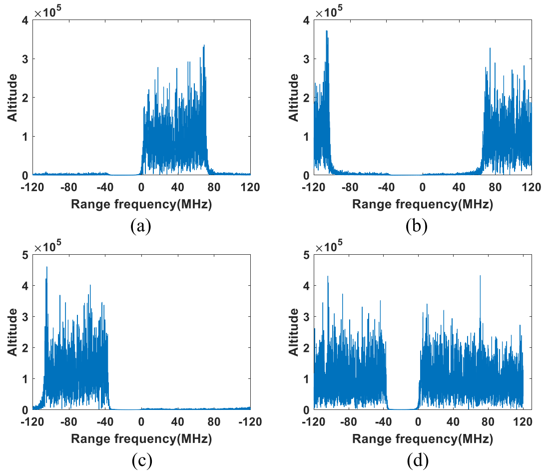

Fig. 7. Echoes from first range region of 1000th pulse in range frequency domain after transmit beamforming in subarray. (a) Spectrum corresponding to first subarray. (b) Spectrum corresponding to second subarray. (c) Spectrum corresponding to third subarray. (d) Spectrum after splicing.

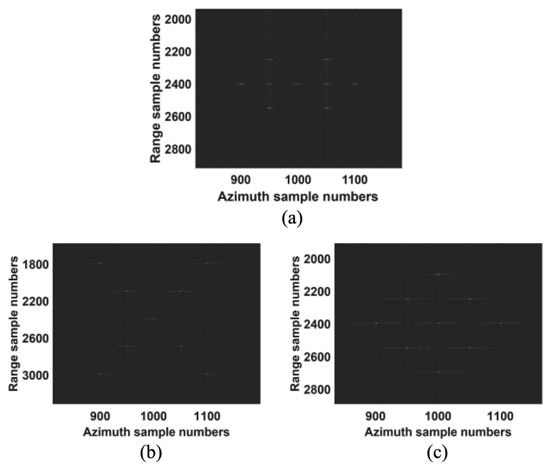

Fig. 8 HRWS Imaging results. (a) First range region. (b) Second range region. (c) Third range region.

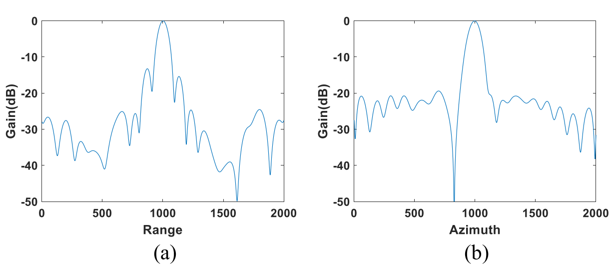

Fig. 9. Profile of the target in first range region. (a) Range profile. (b) Azimuth profile.

B. Imaging Simulations on Distributed Targets

In Fig. 10, we implement experiments on two complex scenes with distributed targets, where the sampling numbers in range and angle domain are 4000 and 2000, respectively. The distributed target consists of 90 000 scattering points, namely, 300 range bins $\times$ 300 azimuth bins. The SAR data used in this part is simulated by using the amplitude

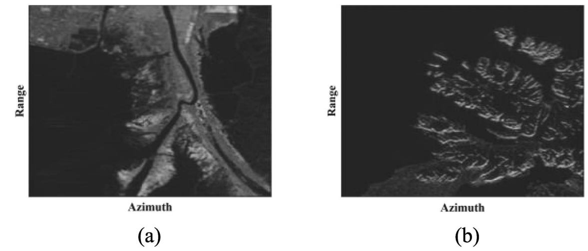

Fig. 10. Distributed targets simulation of original scene. (a) First range region. (b) Second range region.

TABLE II
System Parameters

Symbol	Parameter	Value
f_0	Carrier frequency	5.3 GHz
B_0	Bandwidth	45 MHz
Δf_K	Frequency increment in subarray	1 MHz
Δf_Q	Frequency increment between adjacent subarray	45 MHz
F_r	Fast time sampling frequency	150 MHz
prf	Pulse repetition frequency	4400 Hz
B_d	Doppler bandwidth	3800 Hz
v	Platform velocity	7600 m/s
H	Platform Height	530 Km

information of the measured SAR image. Table II lists the key parameters of the sub-band FDA system used in this part.

Case I: Free of range ambiguity, $Q = 3$, $K = 1$, $\Delta f_Q = B_0 = 45$ MHz. By performing spectrum splicing, three signals with the bandwidth of 45 MHz are synthesized into a signal with the bandwidth of 135 MHz, and then high-resolution SAR imaging can be obtained, as shown in Fig 11. Compared with Fig. 10(a), it is shown the proposed method can achieve high range resolution imaging by spectrum splicing. Fig 11(a) and (b) shows the imaging results with the imperfect orthogonal waveform and ideal orthogonal waveform, respectively. In this article, the ideal orthogonal waveform refers to the waveforms whose cross-correlation energy are completely zero. Imperfect orthogonal waveform refers to the orthogonal waveform in actual, i.e., the cross-correlation energy is not zero. In the simulation, the echoes of ideal orthogonal waveform corresponding to each transmit channel is simulated separately, while the echoes of imperfect waveform corresponding to each transmitting channel is separated by matched filtering. It is concluded that the imaging result of imperfect orthogonal waveform is almost the same as that of the ideal one. Fig. 11(c) shows the range profiles of 1000th azimuth bin with different signals. The distributed targets locate in the area from 1850th to 2150th range bin, where three lines almost overlap together in Fig. 11(c). This is because three imperfect orthogonal waveforms

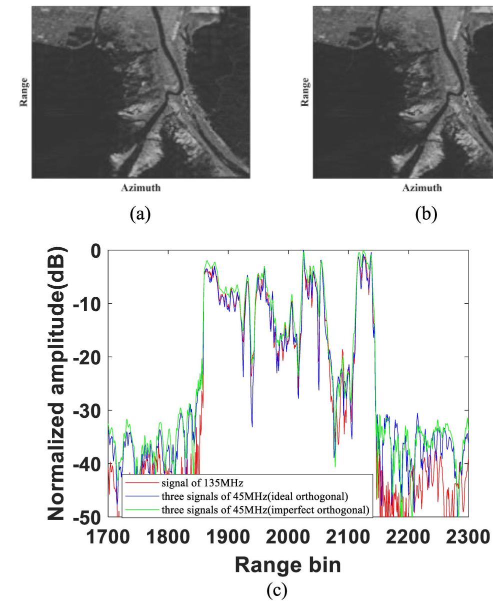

Fig. 11. Waveform comparison of high-resolution SAR imaging by spectrum splicing. (a) SAR imaging results by spectrum splicing using imperfect orthogonal waveform. (b) SAR imaging results by spectrum splicing using ideal orthogonal waveform. (c) Range profile of 1000th azimuth bin (red line: the imaging result with a signal of 135 MHz by traditional single channel method, blue line: the imaging result with three ideal orthogonal signals of 45 MHz by proposed method, green line: the imaging result with three imperfect orthogonal signals of 45 MHz by proposed method).

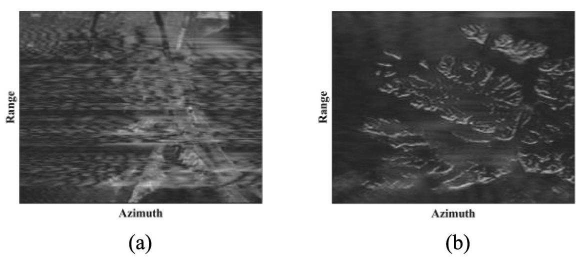

Fig. 12. Imaging results of different range regions with traditional method. (a) First range region. (b) Second range region.

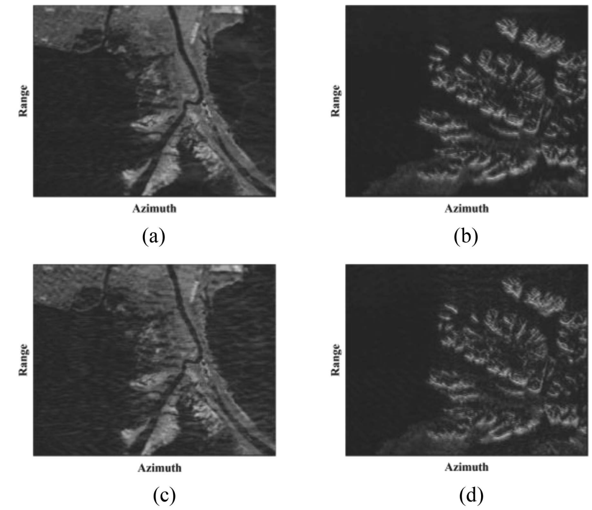

Fig. 13. HRWS imaging results of different range regions with proposed method. (a) Imaging result of first range region using ideal orthogonal waveform. (b) Imaging result of second range region using ideal orthogonal waveform. (c) Imaging result of first range region using imperfect orthogonal waveform. (d) Imaging result of second range region using imperfect orthogonal waveform.

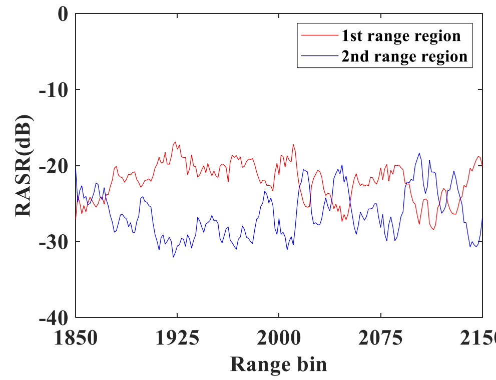

Fig. 14. RASR as a function of the slant range for imaging two range regions.

occupy different frequency bands, and the resulting cross-correlation energy is quite low. Moreover, the imaging results of imperfect orthogonal waveform are similar with the ideal orthogonal waveform.

Case II: With range ambiguity, $Q = 3$, $K = 4$, $\Delta f_Q = B_0 = 45$ MHz, $\Delta f_K = 1$MHz. Fig. 12(a) and (b) presents the imaging results of the first and second range regions, respectively, by traditional SAR imaging algorithm without range ambiguity resolution. We can see that some real scenes are covered by the range ambiguous energy. Fig. 13(a)–(d) shows the HRWS imaging results of the whole scene by the proposed method with ideal and imperfect orthogonal waveforms, respectively. From Fig. 13, we can observe that the ambiguous energy has been suppressed by transmit beamforming. Compared Fig. 13(a), (b) with Fig. 13(c), (d), we see that the cross-correlation energy after matched filtering leads to the degradation of imaging quality.

The performance of the range ambiguity suppression can be evaluated by the range ambiguity to signal ratio (RASR), which is defined as the ratio of the range-ambiguous signal power to the desired signal power [37]. Fig. 14 shows the RASR as a function of the slant range when the proposed method is used for imaging different range regions. We can observe that the RASR for the first and second range region are under -17 dB, which indicates the proposed method has good performance on range ambiguity suppression.

Fig. 15 shows the HRWS imaging results of the first and second range regions by the up-down chirp modulation method [36] and FDA-SAR [19]. The up-down chirp modulation method utilizes the difference of echo sequences in different range regions to separate the range ambiguity echoes. However, the ambiguity energy of up-down chirp

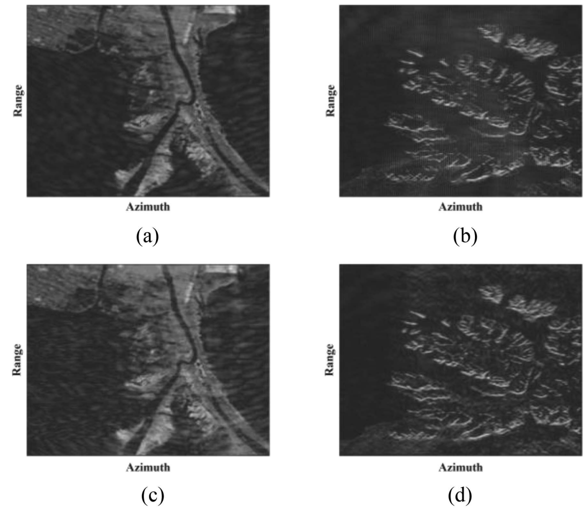

Fig. 15. HRWS imaging results of different range regions with up-down chirp modulation [36] and FDA [19]. (a) Imaging result of first range region with up-down chirp modulation. (b) Imaging result of second range region with up-down chirp modulation. (c) Imaging result of first range region with FDA. (d) Imaging result of second range region with FDA.

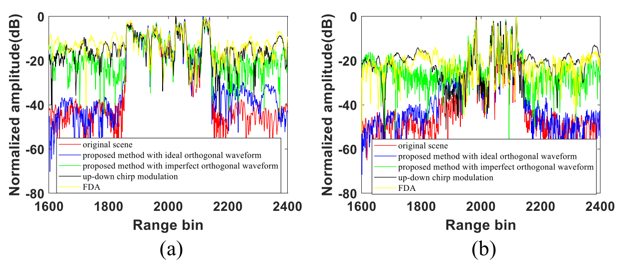

Fig. 16. Range profile comparison of 1000th azimuth bin (red line: the range profile of original scene, blue line: the range profile of imaging results by proposed method with ideal orthogonal waveforms, green line: the range profile of imaging results by proposed method with imperfect orthogonal waveforms, black line: the range profile of imaging results by up-down chirp modulation, yellow line: the range profile of imaging results by FDA-SAR.) (a) First range region. (b) Second range region.

modulation method is not reduced, and it will be defocused along the range. It can be seen in Fig. 15(a) and (b) that the up-down chirp modulation methods suffer from the problem of undesired energy diffusion in the range domain. The FDA-SAR is capable of separating the range ambiguous echoes by utilizing the degrees of freedom in the transmitter, which also suffers from the problem of undesired energy diffusion in the range domain.

The range profiles of 1000th azimuth bin in the first and the second range regions are shown in Fig. 16(a) and (b), respectively. The imaging result corresponding to the proposed method with ideal orthogonal waveform is similar to original scene, which demonstrates the effectiveness of the proposed method on range ambiguous energy suppression. Under practical quasi-orthogonal waveform condition, the proposed sub-band FDA has slight performance improvement over the conventional FDA and up-down chirp modulation methods.

V. CONCLUSION

In this article, a novel sub-band FDA framework is studied for HRWS SAR imaging, to realize wide unambiguous swath coverage and superhigh resolution imaging. By exploiting the frequency increment within subarrays, our work enables to separate the range ambiguous echoes in spatial frequency domain. With spectrum shifting and transmit beamforming procedures, the ambiguous echoes are resolved into several unambiguous parts. On the basis of the proposed phase compensation and spectrum splicing methods, the signal with wide bandwidth can be obtained. Finally, we can achieve the HRWS SAR imaging by applying the traditional imaging approach on the reconstructed signals. The simulation results have verified the effectiveness of the proposed method. In addition, the imaging performance of the proposed method is degraded by the cross-correlation energy of nonideal orthogonal waveforms within each subarray. Thus, with imperfect orthogonal waveforms, the improvement for the proposed technique compared to other techniques is very limited. As a future work, we will explore the design of orthogonal waveform with overlapping spectra and moving target indication on this system.

REFERENCES

[1] P. A. Rosen et al., “Synthetic aperture radar interferometry,” *Proc. IEEE*, vol. 88, no. 3, pp. 333–382, Mar. 2000.

[2] A. Moreira, P. Prats-Iraola, M. Younis, G. Krieger, I. Hajnsek, and K. P. Papathanassiou, “A tutorial on synthetic aperture radar,” *IEEE Geosci. Remote Sens. Mag.*, vol. 1, no. 1, pp. 6–43, Mar. 2013.

[3] M. Suess, B. Grafmueller, and R. Zahn, “A novel high resolution, wide swath SAR system,” in *Proc. IGARSS, Scanning Present Resolving Future, Proc. IEEE Int. Geosci. Remote Sens. Symp. (Cat. No.01CH37217)*, 2001, vol. 3, pp. 1013–1015.

[4] L. Zhang et al., “Adaptive two-step calibration for high resolution and wide-swath SAR imaging,” *IET Radar Sonar Navigation*, vol. 4, no. 4, pp. 548–559, 2010.

[5] L. Zhang, H. Li, Z. Qiao, and Z. Xu, “A fast BP algorithm with wavenumber spectrum fusion for high-resolution spotlight SAR imaging,” *IEEE Geosci. Remote Sens. Lett.*, vol. 11, no. 9, pp. 1460–1464, Sep. 2014.

[6] D. Cohen, D. Cohen, and Y. C. Eldar, “High resolution FDMA MIMO radar,” *IEEE Trans. Aerosp. Electron. Syst.*, vol. 56, no. 4, pp. 2806–2822, Aug. 2020.

[7] A. Currie and M. A. Brown, “Wide-swath SAR. Radar and signal processing,” *IEE Proc. F (Radar Signal Process.)*, vol. 139, no. 2, pp. 122–135, 1992.

[8] G. Krieger, N. Gebert, and A. Moreira, “Unambiguous SAR signal reconstruction from nonuniform displaced phase center sampling,” *IEEE Geosci. Remote Sens. Lett.*, vol. 1, no. 4, pp. 260–264, Oct. 2004.

[9] Z. Li, H. Wang, T. Su, and Z. Bao, “Generation of wide-swath and high-resolution SAR images from multichannel small spaceborne SAR systems,” *IEEE Geosci. Remote Sens. Lett.*, vol. 2, no. 1, pp. 82–86, Jan. 2005.

[10] S. Zhang, M. Xing, X. Xia, J. Li, R. Guo, and Z. Bao, “A robust imaging algorithm for squint mode multi-channel high-resolution and wide-swath SAR with hybrid baseline and fluctuant terrain,” *IEEE J. Sel. Topics Signal Process.*, vol. 9, no. 8, pp. 1583–1598, Dec. 2015.

[11] S. Zhang, S. Li, Y. Liu, M. Xing, and J. Chen, “A novel azimuth Doppler signal reconstruction approach for the GEO-LEO bi-static multi-channel HRWS SAR system,” *IEEE Access*, vol. 7, pp. 39539–39546, 2019.

[12] F. Bordoni, G. Krieger, and M. Younis, “Multifrequency subpulse SAR: Exploiting chirp bandwidth for an increased coverage,” *IEEE Geosci. Remote Sens. Lett.*, vol. 16, no. 1, pp. 40–44, Jan. 2019.
[13] J. Dall and A. Kusk, “Azimuth phase coding for range ambiguity suppression in SAR,” in *Proc. IEEE Int. Geosci. Remote Sens. Symp.*, 2004, vol. 3, pp. 1734–1737.
[14] D. Cristallini, M. Sedehi, and P. Lombardo, “SAR imaging solutions based on azimuth phase coding,” in *Proc. 7th Eur. Conf. Synthetic Aperture Radar*, 2008, pp. 1–4.
[15] J. Yang, G. Sun, Y. Wu, and M. Xing, “Range ambiguity suppression by azimuth phase coding in multichannel SAR systems,” in *Proc. IET Int. Radar Conf.*, 2013, pp. 1–5, doi: 10.1049/cp.2013.0197.
[16] W. Xu, P. Huang, and W. Tan, “Azimuth phase coding by up and down chirp modulation for range ambiguity suppression,” *IEEE Access*, vol. 7, pp. 143780–143791, 2019.
[17] L. Jian et al., “A two-dimensional phase coding for range ambiguity suppression [J],” *Digit. Signal Process.*, vol. 81, pp. 155–162, 2018.
[18] X. He, G. Liao, S. Zhu, J. Xu, and C. Wang, “Range-Ambiguous clutter suppression for the SAR-GMTI system based on extended azimuth phase coding,” *IEEE Trans. Geosci. Remote Sens.*, vol. 58, no. 11, pp. 8147–8162, Nov. 2020.
[19] C. Wang, J. Xu, G. Liao, X. Xu, and Y. Zhang, “A range ambiguity resolution approach for high-resolution and wide-swath SAR imaging using frequency diverse array,” *IEEE J. Sel. Topics Signal Process.*, vol. 11, no. 2, pp. 336–346, Mar. 2017.
[20] J. Xu, G. Liao, and H. C. So, “Space-Time adaptive processing with vertical frequency diverse array for range-ambiguous clutter suppression,” *IEEE Trans. Geosci. Remote Sens.*, vol. 54, no. 9, pp. 5352–5364, Sep. 2016.
[21] J. Xu, S. Zhu, and G. Liao, “Range ambiguous clutter suppression for airborne FDA-STAP radar,” *IEEE J. Sel. Topics Signal Process.*, vol. 9, no. 8, pp. 1620–1631, Dec. 2015.
[22] L. Lan, G. Liao, J. Xu, Y. Zhang, and B. Liao, “Transceive beamforming with accurate nulling in FDA-MIMO radar for imaging,” *IEEE Trans. Geosci. Remote Sens.*, vol. 58, no. 6, pp. 4145–4159, Jun. 2020.
[23] K. V. Mishra, Y. C. Eldar, E. Shoshan, M. Namer, and M. Meltsin, “A cognitive sub-nyquist MIMO radar prototype,” *IEEE Trans. Aerosp. Electron. Syst.*, vol. 56, no. 2, pp. 937–955, Apr. 2020.
[24] G. Krieger, “MIMO-SAR: Opportunities and pitfalls,” *IEEE Trans. Geosci. Remote Sens.*, vol. 52, no. 5, pp. 2628–2645, May 2014.
[25] H. Wang et al., “A novel range ambiguity resolving approach for high-resolution and wide-swath SAR imaging utilizing space-pulse phase coding - ScienceDirect[J],” *Signal Process.*, vol. 168, pp. 107323–107323, Mar. 2020.
[26] H. Wang et al., “Study on coding scheme for space-pulse-phase-coding-based high-resolution and wide-swath SAR imaging,” *Int. J. Remote Sens.*, vol. 41, no. 18, pp. 7186–7200, 2020.
[27] J. Xu, Y. Zhang, G. Liao, and H. Cheung So, “Resolving range ambiguity via multiple-input multiple-output radar with element-pulse coding,” *IEEE Trans. Signal Process.*, vol. 68, pp. 2770–2783, Apr. 2020.
[28] S. Welstead, “Characterization of diversity approaches for LFM stretch-processed waveforms,” in *Proc. Int. Waveform Diversity Des. Conf.*, 2007, pp. 418–422.
[29] W. Wang, “MIMO SAR chirp modulation diversity waveform design,” *IEEE Geosci. Remote Sens. Lett.*, vol. 11, no. 9, pp. 1644–1648, Sep. 2014.
[30] G. Jin, W. Wang, Y. Deng, H. Yan, and R. Wang, “A novel range-azimuth joint modulation scheme for range ambiguity suppression,” *IEEE Trans. Geosci. Remote Sens.*, vol. 60, May 2021, Art. no. 5207210.
[31] G. Jin et al., “An advanced nonlinear frequency modulation waveform for radar imaging with low sidelobe,” *IEEE Trans. Geosci. Remote Sens.*, vol. 57, no. 8, pp. 6155–6168, Aug. 2019.
[32] J. Wang, L. Chen, X. Liang, C. Ding, and K. Li, “Implementation of the OFDM chirp waveform on MIMO SAR systems,” *IEEE Trans. Geosci. Remote Sens.*, vol. 53, no. 9, pp. 5218–5228, Sep. 2015.
[33] S. Sen, “PAPR-Constrained Pareto-optimal waveform design for OFDM-STAP radar,” *IEEE Trans. Geosci. Remote Sens.*, vol. 52, no. 6, pp. 3658–3669, Jun. 2014.
[34] K. Kauffman, J. Raquet, Y. Morton, and D. Garmatyuk, “Real-Time UWB-OFDM radar-based navigation in unknown terrain,” *IEEE Trans. Aerosp. Electron. Syst.*, vol. 49, no. 3, pp. 1453–1466, Jul. 2013.
[35] G. Jin, Y. Deng, W. Wang, R. Wang, Y. Zhang, and Y. Long, “Segmented phase code waveforms: A novel radar waveform for spaceborne MIMO-SAR,” *IEEE Trans. Geosci. Remote Sens.*, vol. 59, no. 7, pp. 5764–5779, Jul. 2021.
[36] J. Mittermayer and J. M. Martinez, “Analysis of range ambiguity suppression in SAR by up and down chirp modulation for point and distributed targets,” in *Proc. IEEE Int. Geosci. Remote Sens. Symp. Proc. (IEEE Cat. No.03CH37477)*, 2003, vol. 6, pp. 4077–4079.
[37] G. Jin et al., “New insights into SAR alternate transmitting mode based on waveform diversity,” *IEEE Trans. Geosci. Remote Sens.*, vol. 60, May 2021, Art no. 5209209.

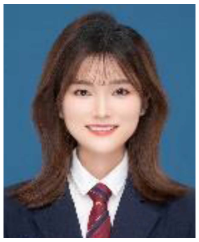

Mengdi Zhang was born in Shaanxi, China, in 1994. She received the B.S. degree in electronic engineering and the Ph.D. degree in signal and information processing from Xidian University, Xi’an, China, in 2016 and 2021, respectively.

February 2022, she is currently a Lecturer with the School of Information and Control Engineering, China University of Mining and Technology. Her research interests include synthetic aperture radar, high-resolution and wide-swath imaging, and waveform diverse array radar.

Guisheng Liao (Senior Member, IEEE) was born in Guilin, China, in 1963. He received the B.S. degree in mathematics from Guangxi University, Guangxi, China, in 1985, and the M.S. and Ph.D. degrees in signal and information processing from Xidian University, Xi’an, China, in 1990 and 1992, respectively.

He is currently a Yangtze River Scholars Distinguished Professor with the National Laboratory of Radar Signal Processing and was the Dean with the School of Electronic Engineering, Xidian University. Since 2009, he has been the evaluation expert for the international cooperation project of Ministry of Science and Technology in China. Since 2007, he has been the lead of Yangtze River Scholars Innovative Team and devoted in advanced techniques in signal and information processing. Since 2006, he has been the panelists for the medium and long term development plan in high-resolution and remote sensing systems. From 1999 to 2000, he was a Senior Visiting Scholar with the Chinese University of Hong Kong, Hong Kong. His research interests include array signal processing, space-time adaptive processing, radar waveform design, airborne/space surveillance, and warning radar systems.

Jingwei Xu (Member, IEEE) was born in Shandong, China. He received the B.S. degree in electronic engineering and the Ph.D. degree in signal and information processing from Xidian University, Xi’an, China, in 2010 and 2015, respectively.

He is currently an Associated Professor with the School of Electronic Engineering, Xidian University. From 2015 to 2017, he was a Lecturer with the National Lab of Radar Signal Processing, Xidian University. From 2017 to 2019, he was a Postdoctoral Fellow under “Hong Kong Scholar Program” with the City University of Hong Kong.

His research interests include radar system modeling, multisensor array signal processing, space-time adaptive processing, multiple-input multiple-output radar, and waveform diverse array radar.

Xiongpeng He was born in Shaanxi, China, in 1992. He received the B.S. degree in electronic engineering and the Ph.D. degree in signal and information processing from Xidian University, Xi'an, China, in 2015 and 2020, respectively.

From November 2020, he is a Tenure-track Associated Professor with the National Laboratory of Radar Signal Processing, Xidian University. His research interests include synthetic aperture radar, ground moving target indication, radar transmit diversity, and space-time adaptive processing.

Qi Liu (Member, IEEE) received the bachelor's and master's degrees in material science and chemical engineering from Harbin Engineering University, Harbin, China, in 2013 and 2016, respectively, and the Ph.D. degree in electrical engineering from City University of Hong Kong, Hong Kong, China, in 2019.

He is currently a Professor with the School of Future Technology, South China University of Technology. During 2018–2019, he was a Visiting Scholar with the University of California Davis, CA, USA. From 2019 to 2022, he was a Research Fellow with the Department of Electrical and Computer Engineering, National University of Singapore, Singapore. His research interests include machine learning, optimization methods, and neuromorphic computing with applications to image/video/speech signal processing.

Dr. Liu is an Associate Editor for the IEEE SYSTEMS JOURNAL (2022-), and *Digital Signal Processing* (2022-). He was also Guest Editor for the *International Journal of Antennas and Propagation*, and *Wireless Communications and Mobile Computing*. He was the recipient of the Best Paper Award of *IEEE International Conference on Signal, Information and Data Processing* in 2019.

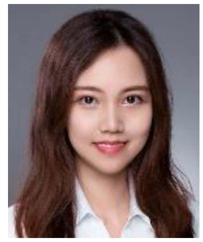

Lan Lan (Member, IEEE) was born in Xi'an, China, in 1993. She received the B.S. degree in electronic engineering and the Ph.D. degree in signal and information processing from Xidian University, Xi'an, China, in 2015 and 2020, respectively.

From July 2019 to July 2020, she was a visiting Ph.D. student with the University of Naples Federico II, Naples, Italy. From August 2020, she is currently a Tenure-track Associated Professor with the National Laboratory of Radar Signal Processing, Xidian University. She was elected as the "Youth Elite Scientist Sponsorship Program" by China Association for Science and Technology in 2022. She was a recipient of the Excellent Paper Award at the CIE 2016 International Conference on Radar. She is currently with the editorial boards of Digital Signal Processing. Her research interests include frequency diverse array radar systems, MIMO radar signal processing, target detection, and ECCM.

Shiyin Li was born in Sichuan, China, in 1971. He received the Ph.D. degree in information and communication engineering from the China University of Mining and Technology, Xuzhou, China, in 2010.

Since 2010, he has been a Professor with the School of Information and Control Engineering, China University of Mining and Technology. He is currently the Vice Dean with the School of Information and Control Engineering. His research interests include wireless communication and indoor localization.